ADVANCED MATERIALS
www.advmat.de

Biodegradable Polymer with Effective Near-Infrared-II Absorption as a Photothermal Agent for Deep Tumor Therapy

Yingjie Yu, Dongsheng Tang, Chaoyong Liu, Qi Zhang, Lin Tang, Yunfeng Lu,* and Haihua Xiao**

Photothermal therapy holds great promise for cancer treatment due to its effective tumor ablation and minimal invasiveness. Herein a new class of biodegradable photothermal agents with effective adsorption in both near-infrared-I (NIR-I) and NIR-II windows is reported for deep tumor therapy. As demonstrated in a deep-seated ovarian cancer model, photothermal therapy using 1064 nm irradiation effectively inhibits tumor progression and prolongs survival spans. This work provides a new design of photothermal agents toward a more effective therapy of tumors.

1. Introduction

Photothermal therapy (PTT), which relies on photothermal agents (PTAs) delivered to tumor sites to adsorb light irradiation and converse photoenergy into heat for tumor ablation, has drawn extensive attention owing to its ability to eradicate tumors noninvasively.[1] Based on the clinical needs, the criteria for ideal PTA are shown as follows: 1) good biodegradability, 2) good photostability, 3) strong absorption in the NIR region for tissue penetration, 4) high photothermal conversion efficiency (PCE).[2] Preclinical studies and early phase trials of PTT have demonstrated promising therapeutic efficacy for superficial tumors (e.g., skin, head, and neck cancer);[3] its use for deep tumors (e.g., lung cancer and ovarian cancer), however, is hampered by several key factors, such as effective delivery of PTAs to tumor sites, the biocompatibility of PTAs, adsorption, and conversion of photoenergy through deep tissues.[4] Generally, light with a wavelength in the near-infrared-II window (NIR-II, 1000–1700 nm) could provide a deeper tissue-penetration length (≈ 5 mm) with less scattering and tissue absorption,[5] compared with light in the near-infrared-I window (NIR-I, 650–950 nm) with a tissue penetration depth of less than 1 mm.[6] Developing PTAs with high biocompatibility, adsorption in the NIR-II window, and photoenergy-conversion efficiency, in this context, is essential toward PTT for deep tumors.

Current NIR-II PTAs are mainly based on inorganic particles (e.g., gold nanoparticles, copper sulfide, and black phosphorus),[7] which are generally non-degradable under physiological conditions. Despite that some studies have claimed biodegradability for such materials, the degradation mechanisms are unclear, and balancing the degradability and photothermal performance of such materials remains difficult.[8] Organic dyes have also been explored,[9] whereas their poor photostability could limit their use as effective NIR-II PTAs.[10] Conjugated polymer, which affords strong absorption in the NIR-II window and excellent photostability,[6a,11,12] is highly promising PTAs; however, such materials are inherently nondegradable under physiological conditions.[13] Most research in polymeric PTAs has been focused on photothermal performance; little attention was paid to their biodegradability.[14]

Herein, we report a novel class of biodegradable polymeric PTAs through incorporating a flexible unit containing disulfide bonds into the conjugated backbones. To distinguish it with traditional conjugated polymer, we name this new type of polymer as "pseudo-conjugated polymers". Disulfide bonds are cleavable by glutathione (GSH), the most abundant thiol in animal cells, of which the concentration in tumor cells is generally 100–1000 times higher than that in normal cells.[15] As illustrated

Y. Yu, D. Tang, C. Liu, L. Tang
State Key Laboratory of Organic-Inorganic Composites
Beijing Laboratory of Biomedical Materials
Beijing Advanced Innovation Center for Soft Matter Science and Engineering
College of Life Science and Technology
Beijing University of Chemical Technology
Beijing 100029, P. R. China
E-mail: chaoyongliu@mail.buct.edu.cn

D. Tang, H. Xiao
Beijing National Laboratory for Molecular Science
State Key Laboratory of Polymer Physical and Chemistry
Institute of Chemistry
Chinese Academy of Science
Beijing 100190, China
E-mail: hhxiao@iccas.ac.cn

D. Tang, H. Xiao
University of Chinese Academy of Science
Beijing 100049, China

Q. Zhang
Department of Chemistry
University of Michigan
Ann Arbor, MI 48109, USA

Y. Lu
Department of Chemical and Biomolecular Engineering
University of California, Los Angeles
Los Angeles, CA 90095, USA
E-mail: luucla@ucla.edu

The ORCID identification number(s) for the author(s) of this article can be found under https://doi.org/10.1002/adma.202105976.

DOI: 10.1002/adma.202105976

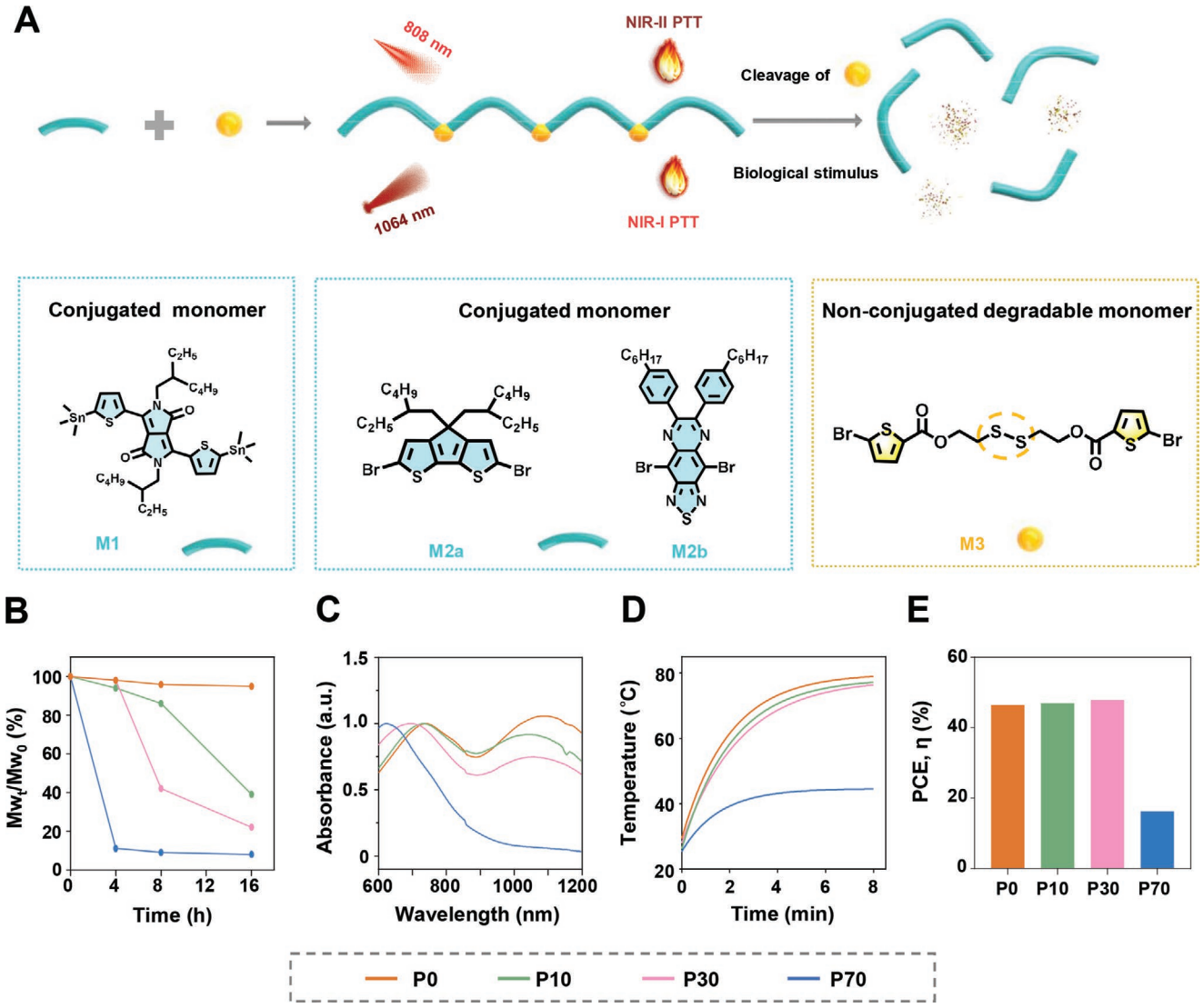

Figure 1. Synthesis of biodegradable PTAs. A) Schematic illustration of the synthesis of biodegradable PTAs by the Stille polycondensation of tin-containing conjugated monomer (M1) and bromine-containing monomers (M2a, M2b, and M3). B) Degradation of PTAs in 10×10^{-3} M GSH estimated by the change of M_w represented by M_{wt}/M_{w0}. C) UV–vis spectra of the PTAs (25 μg mL^{-1}). D) Temperature profiles of PTA solutions (200 μg mL^{-1}) after 1064 nm laser irradiation. E) Photothermal conversion efficiency (PCE) of PTAs with different molar ratios of M3 upon 1064 nm irradiation.

in **Figure 1**A and Scheme S1 (Supporting Information), such biodegradable PTAs are synthesized through the Stille polycondensation of tin-containing conjugated monomer (M1) and bromine-containing monomers (M2a, M2b, and M3), where M3 is the degradable disulfide monomer (see Scheme S2, Figures S1 and S2, Supporting Information for the synthesis and characterization). A series of PTAs were synthesized with different molar percentages of M3 in the bromine-containing monomers (*z*), which are denoted as P(*z*), and characterized by ^{1}H NMR (Figures S3–S6, Supporting Information) and gel permeation chromatography (GPC) analysis. Their composition and molecular weight (M_w) are summarized in Table S1 (Supporting Information). Notably, in such a system, the conjugated section endows the system with photothermal properties, whereas the non-conjugated section endows biodegradability.

2. Results and Discussion

The biodegradation process of the polymer was accessed by the change of M_w during incubation at 37 °C with 10×10^{-3} M GSH, a concentration mimicking the GSH concentration in the tumor-cell environment.[16] Figure 1B compares the change of the M_w estimated by M_{wt}/M_{w0}, where M_{w0} is the initial M_w and M_{wt} is the M_w after different incubation time. P0 exhibits an insignificant change in M_w after 16 h, whereas with increasing M3 ratio, P10, P30, and P70 show an increasing degree of degradation, indicating tunable degradation kinetics (Figure 1B). Figure 1C shows the UV–vis spectra of the polymers in chloroform. P0, P10, and P30 exhibit similar absorbances at both NIR-I (≈740 nm) and NIR-II window (≈1089 nm), whereas P70 shows only an absorption peak in the NIR-I window (624 nm).

Irradiating the solutions of P0, P10, and P30 (200 μg mL^{-1}) with 1064 nm laser light rapidly increases solution temperature to near 80 °C (Figure 1D) with a similar photothermal conversion efficiency (PCE) of ≈47% (Figure 1E). In contrast, irradiating the solution of P70 leads to a much lower solution temperature (≈40 °C), attributed to the shorter conjugation length. Consistently, P0 and P30 exhibit a similar energy gap between their lowest unoccupied molecular orbital (LUMO) and highest occupied molecular orbital (HOMO) (1.13 and 1.31 eV, respectively) (Figure S7, Supporting Information), a value significantly lower than that of P70 (1.52 eV) (Table S2, Supporting Information). These studies suggest that up to 30% of M3 can be incorporated into the conjugative polymers to provide tunable biodegradability without compromising the photothermal performance.

Toward therapeutic applications, P30 was encapsulated within an amphiphilic and biodegradable copolymer via a nanoprecipitation method.[17] Briefly, P30 and methoxy poly(ethylene glycol)$_{5000}$-*b*-poly(lactide-*co*-glycolide)$_{7600}$ (mPEG$_{5000}$-PLGA$_{7600}$) are first dissolved in tetrahydrofuran (THF) with a 10:1 mass ratio; the solution is then added to a mixing solution (9 mL water and 1 mL THF) under continuous sonication, leading to the formation of homogenous nanoparticles denoted hereinafter as NP. As depicted in **Figure 2**A, NP is covered with PEG lengths prolonging their blood circulation time, as incorporated P30 enables effective photothermal conversion, and the disulfide linkers provide degradability upon their intracellular entrance.[18] Figure 2B shows a representative transmission electron microscopy (TEM) image of NP, displaying

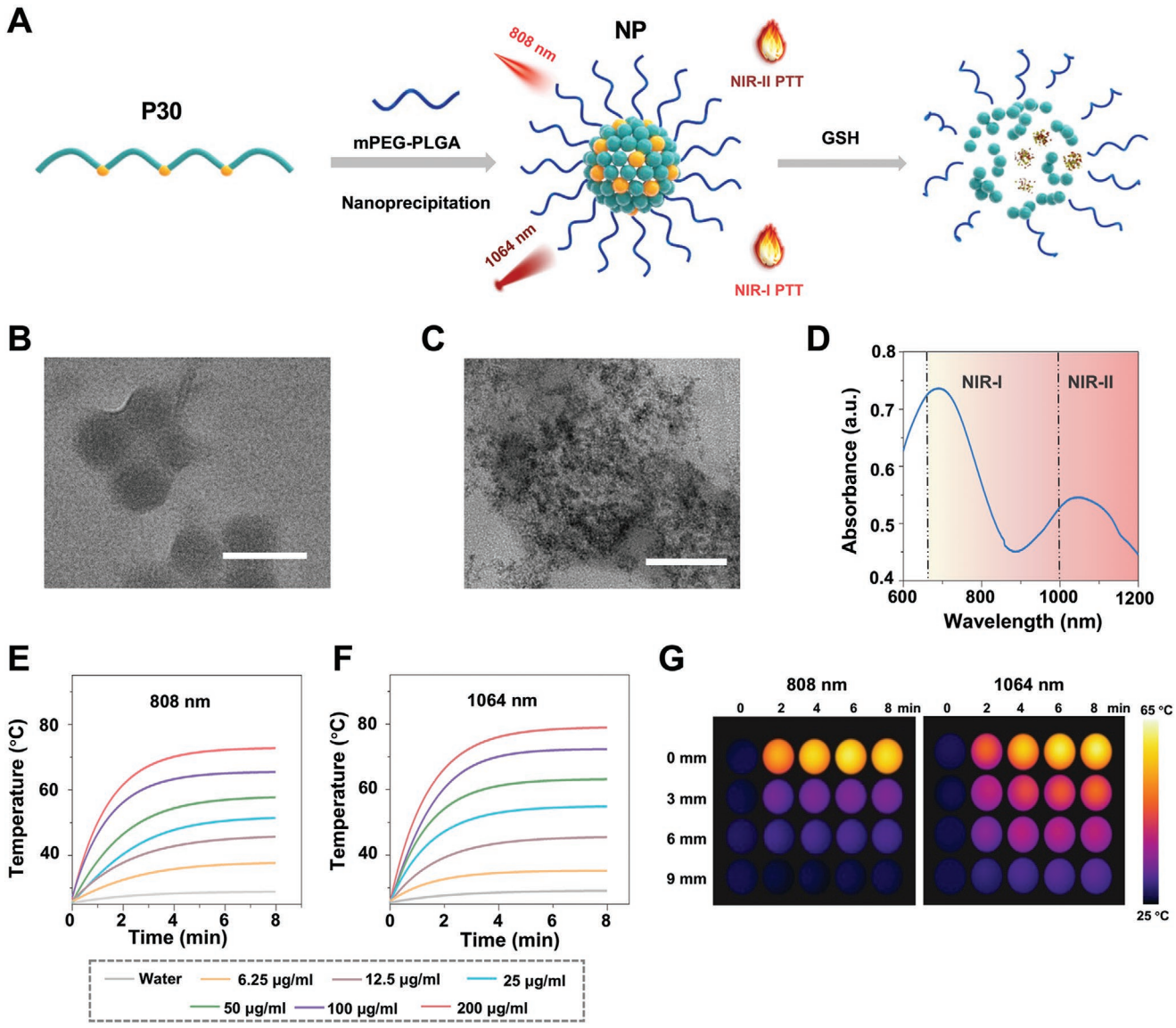

Figure 2. Biodegradability and photothermal conversion of NP. A) Schematic illustration for the fabrication of P30-containing NP through a nanoprecipitation method and their degradation in response to GSH. B) TEM image of NP. Scale bar: 100 nm. C) TEM image of NP incubated with GSH (10 × 10^{-3} M) for 6 h. Scale bar: 100 nm. D) UV–vis spectra of NP solution (25 μg mL^{-1} in water). E,F) Temperature profiles of different concentrations of NP solutions under irradiation of 808 nm (E) and 1064 nm (F) laser light. G) Thermal imaging of NP solutions (100 μg mL^{-1}) under 808 and 1064 nm irradiation through a chicken breast with a thickness of 0, 3, 6, and 9 mm, respectively.

spherical morphology with a diameter of ≈60 nm, which is consistent with the dynamic light scattering (DLS) measurement (≈64 nm) (Figure S8, Supporting Information). After incubation with 10×10^{-3} M GSH at 37 °C for 6 h, NP is degraded into small fragments (Figure 2C). This is further confirmed by the DLS study, where degradation of NP leads to large size aggregations (Figure S9, Supporting Information).[17] To further confirm the role of the disulfide bonds in the degradation of NP, nondegradable NP were also synthesized using a P30 analog that contains a similar amount of non-degradable linker (30%) (Schemes S3 and S4 and Figures S10–S12 and Table S3, Supporting Information). Such nondegradable NP exhibit similar size and morphology throughout the treatments, confirming the roles of disulfide bonds in the degradability of NP (Figure S13, Supporting Information).

Figure 2D shows the UV–vis spectra of NP solution (25 μg mL^{-1} in water), which exhibits absorption peaks at NIR-I (693 nm) and NIR-II (1052 nm) windows. It is worth noting that the NP has a similar absorbance at 808 and 1064 nm. The photothermal conversion of NP was examined by monitoring the temperature of NP solutions upon 808 or 1064 nm irradiation. As shown in Figure 2E,F, increasing the NP concentration leads to a faster temperature increase. A high temperature of 73.3 °C and 79.8 °C is achieved with a NP concentration of 200 μg mL^{-1} within 4 min, respectively, suggesting an excellent photothermal conversion (Figure S14, Supporting Information). The PCE value of the NP under 1064 nm irradiation is ≈ 49%, indicating superior photothermal conversion efficiency (Figure S15, Supporting Information).[19] Such photothermal performance is well retained after four testing cycles. Nondegradable NP prepared with fully conjugated polymer P0 was provided for comparison. No obvious difference was observed between them, suggesting the introduction of the nonconjugated section does not affect the photostability of NP[20] (Figure S16, Supporting Information). To examine the effectiveness of NP in deep tissues, chicken breast with a thickness of 3, 6, and 9 mm was placed above the NP solutions (100 μg mL^{-1} in water) (Scheme S5, Supporting Information and Figure 2G). Without

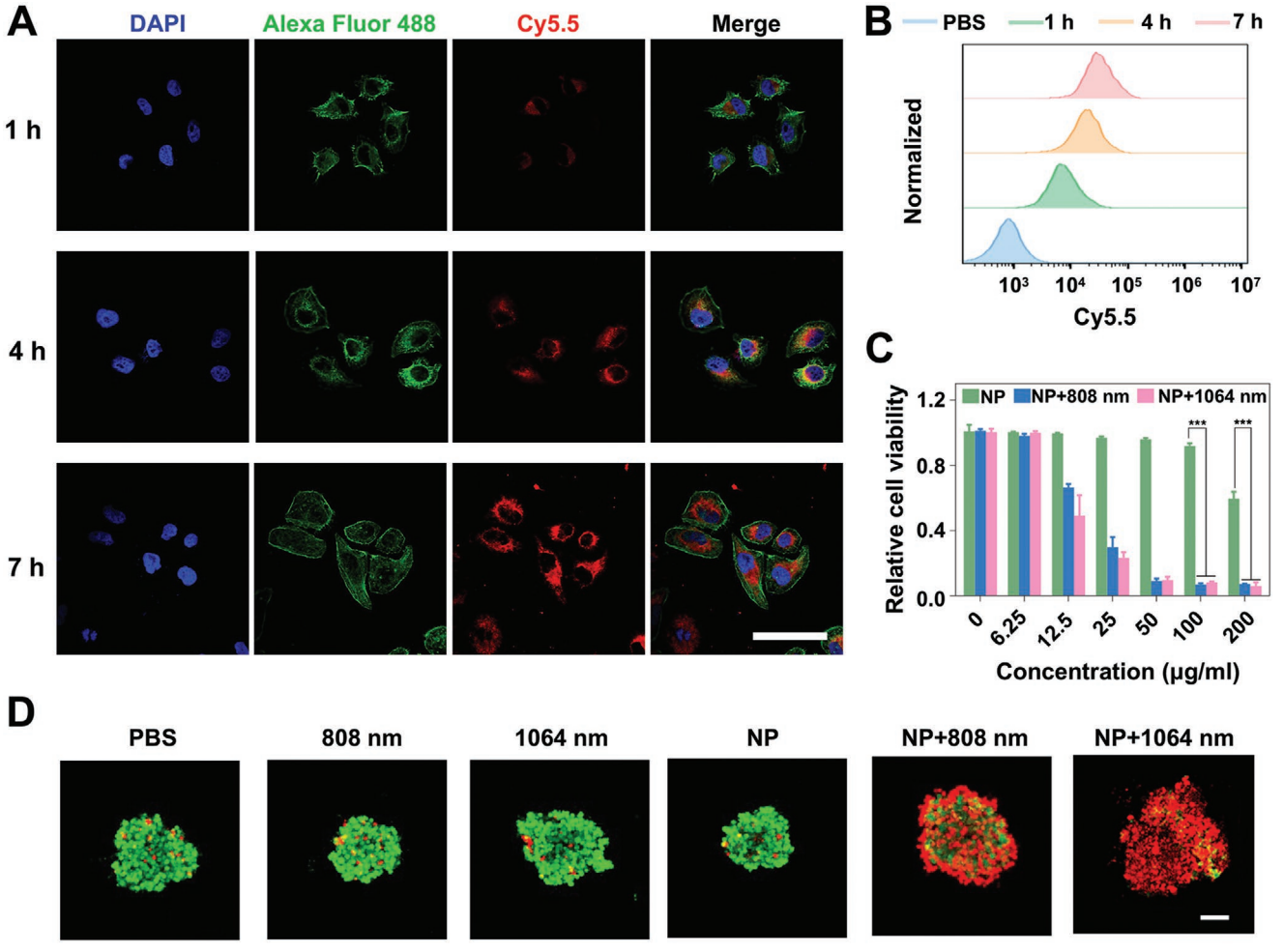

Figure 3. Entrance of NP to cells and their photoablation effects. A) Fluorescence images of OVCAR8 after incubation with Cy5.5-labeled NP for 1, 4, and 7 h, respectively. The red color comes from Cy5.5-labeled NP. The green color comes from the cell actin stained by Alexa Fluor 488. Scale bar: 100 μm. B) Flow cytometry of cells incubated with Cy5.5-labeled NP for 1, 4, and 7 h, respectively. C) Relative viability of OVCAR8 cells after incubation with various concentrations of NP under 808 and 1064 nm irradiation. D) Live/dead cell staining for multicellular spheroids of OVCAR8 after different treatments. Red: dead cells, green: live cells. Scale bar: 100 μm.

the chicken breast, the solution temperature is raised to 62 °C under 808 or 1064 nm irradiation. With the coverage, the solution temperature is respectively raised to 49, 41, and 33 °C with 1064 nm irradiation, which are 1.4, 1.2, and 1.17 times higher than that with 808 nm irradiation (Figure 2G and Figures S17 and S18, Supporting Information). This excellent deep penetration capacity can be attributed to the higher transmittance of the 1064 nm laser light compared with the 808 nm laser light.

High-grade serous ovarian cancer (HGSOC) was used to evaluate the therapeutic efficacy of NP. Notably, HGSOC is the most common and deadliest type of ovarian cancer, which is highly metastatic and diffused deeply in the abdominal cavity. Surgical excision is undesirable and chemotherapy could lead to drug resistance with a 5-year survival rate of 5%.[21] Toward this goal, we first evaluated cell uptake of NP by incubating Cy5.5-labeled NP with OVCAR8 cells for 1, 4, and 7 h. As shown in **Figure 3**A, the cells show the increasing intensity of red fluorescence indicating the cellular entrance of NP, which is confirmed by the flow cytometry (Figure 3B). The photoablative ability of NP was further examined by incubating the cells with different concentrations of NP followed by 808 or 1064 nm irradiation. As shown in Figure 3C, without irradiation, the cells with 100 μg mL^{-1} NP show high cell viability of 92% suggesting insignificant cytotoxicity of NP; with irradiation, the cell viability is rapidly reduced even at a low NP concentration of 12.5 μg mL^{-1}. 3D multicellular tumor spheroids (MCS) were further used to exam

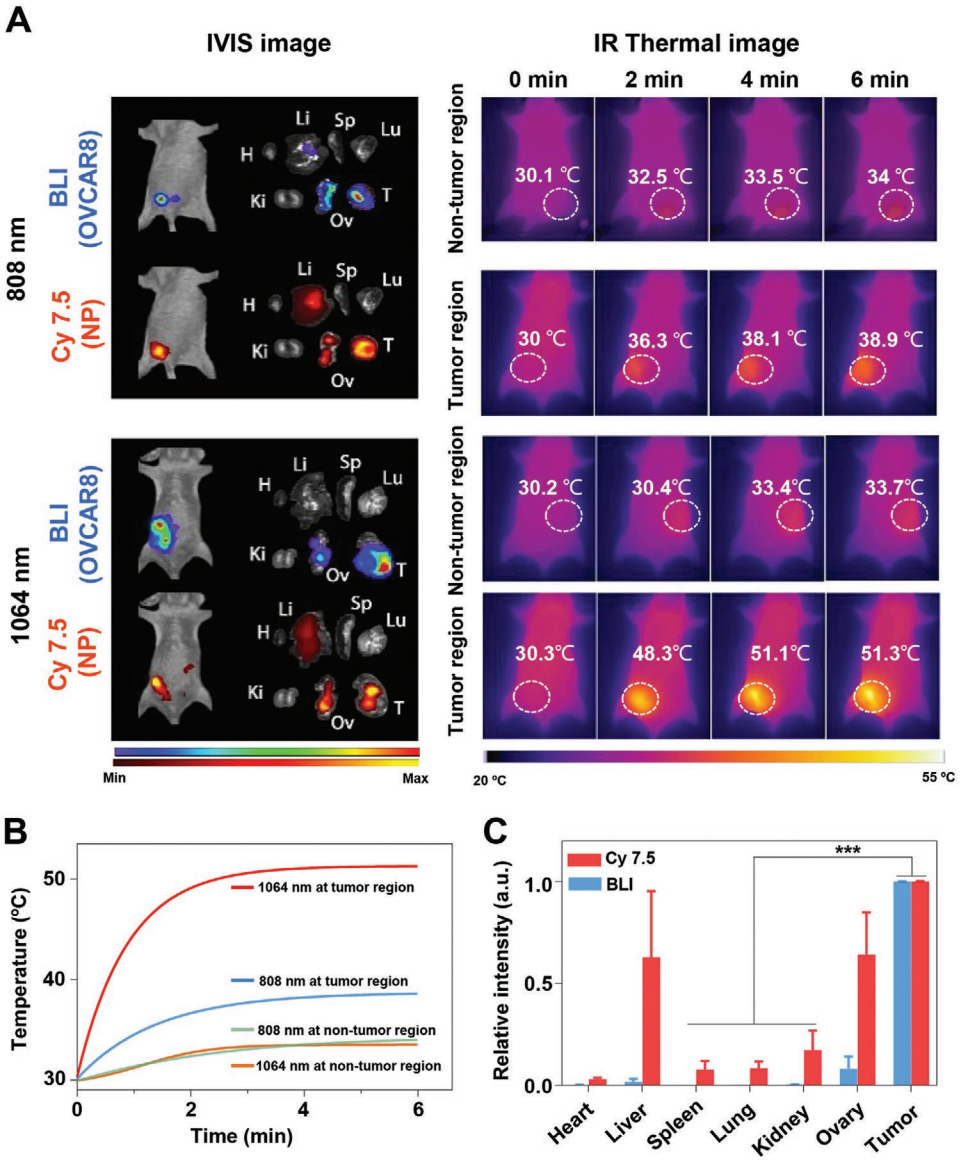

Figure 4. Biodistribution and therapeutic efficacy of NP in ovarian cancer model. A) Left: Biodistribution of Cy7.5-labeled NP, bioluminescence imaging (BLI) of the tumors, and ex vivo fluorescence images of tumors and major organs, including heart (H), liver (Li), spleen (Sp), lung (Lu), kidneys (K), ovaries (O), and tumors (T). Right: Thermal image of the mice upon irradiation with 808 nm and 1064 nm laser light for 6 min. B) Temperature profiles of tumor and non-tumor regions upon irradiation using 808 and 1064 nm laser light. C) Ex vivo fluorescence intensity of the tumor and major organs 24 h post-injection of NP.

the photoablation effect by live/dead cell staining (Figure 3D). The MCS treated with PBS, NP, 808 nm irradiation, or 1064 nm irradiation alone show no sign of apoptosis, whereas MCS with NP under 808 nm irradiation or NP under 1064 nm irradiation shows significant apoptosis, indicating an excellent photoablation effect for tumor cells and tissues.

The therapeutic efficacy was examined by an imaging-guided PTT (Scheme S6, Supporting Information).[22] Briefly, a HGSOC model was established by intraperitoneal (IP) injection of luciferase-expressing OVCAR8 cells (LUC$^+$OVCAR8). Cy7.5-labeled NPs were intraperitoneally injected, and their distribution was imaged 24 h with an in vivo imaging system (IVIS) after the injection.[23] As shown in **Figure 4**A, the tumors are mainly dispersed in the abdominal region, while the NPs are mainly accumulated within the tumor regions. The tumor region is visualized through bioluminescent imaging (BLI), which

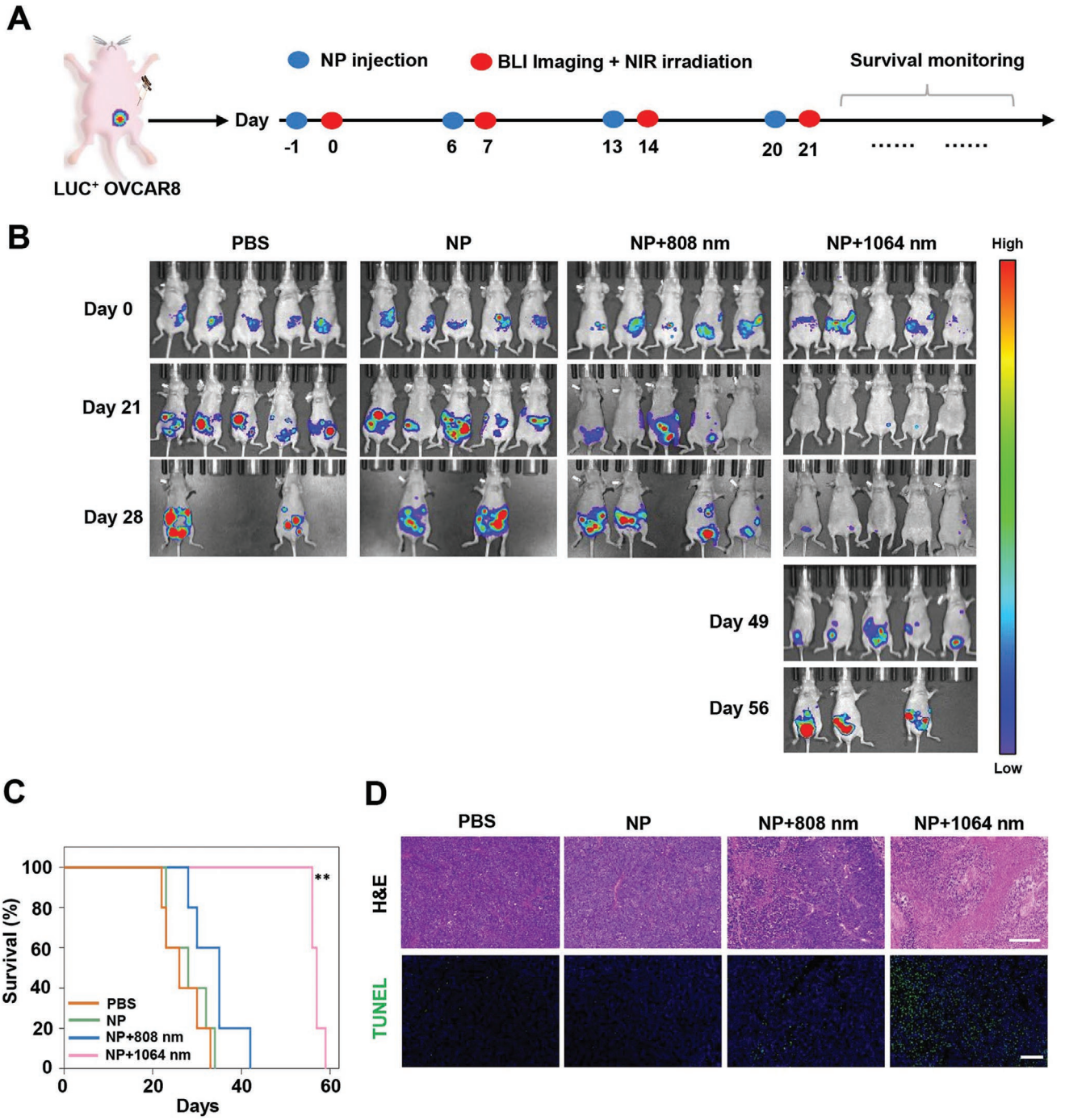

Figure 5. Therapeutic efficacy of NP for deep-seated OVCAR8 ovarian cancer. A) Schematic illustrating the experimental design. B) Growth of LUC$^+$OVCAR8 tumors in mice visualized by IVIS. C) Survival rate of OVCAR8-tumor-bearing mice that received various treatments. $^{**}p < 0.01$ (Log-rank (Mantel–Cox) test). D) H&E staining and TUNEL of the tumor tissues for various treatment groups. Scale bar: 100 µm.

is used to guide the choice of irradiation sites. With irradiation at the tumor region, thermal imaging suggests the tumor regions exhibit a significantly higher temperature than the nontumor regions. Such an effect is even more pronounced under 1064 nm irradiation. Figure 4B provides the quantitative temperature profiles, confirming 1064 and 808 nm irradiation rapidly heats up the tumor regions to 51 °C and 38 °C in 6 min, while nontumor regions only exhibit slight temperature increase from 30.2 °C to 33.7 °C for 1064 nm irradiation or from 30.1 to 34 °C for 808 nm irradiation. The organs were harvested and imaged ex vivo, which confirms the accumulation of NP in the tumors and ovaries (Figure 4C). Taken together, these experiments demonstrate that NP can be delivered and accumulated in the tumor regions via intraperitoneal injection, effectively and selectively increasing the temperate of tumor sites.

PTT was performed on the HGSOC mouse model illustrated in **Figure 5**A. Once the intensity of the LUC signal in the tumors reached 3×10^6 radians (photons/s/cm^2/surface area), NP (200 µL, 500 µg mL^{-1}) was administered by IP injection once a week for 4 weeks. An equal volume of phosphate-buffered saline (PBS) was used as the negative control. Irradiation (808 or 1064 nm) was applied 24 h after the injection to tumor regions and tumor progression was visualized weekly. Figure 5B shows the tumor growth of the mice visualized by IVIS. On day 28, only two from the PBS and NP group survive with large size tumors, four of the group with NP + 808 nm irradiation survive also with large size tumors, while the group with NP + 1064 nm irradiation survive nearly tumor free. During the whole experimental period, the body weights of mice in each group were similar, suggesting no obvious toxicity of NP (Figure S19A, Supporting Information). The growth of the tumors was further quantified by the relative BLI value in the abdominal area (Figure S19B, Supporting Information). As shown in Figure 5C, the PBS and NP groups exhibit a similar growth trend and died within 34 d. The group with NP + 808 nm irradiation also shows rapid tumor growth after the end of the four treatments and died within 42 d. In contrast, the group with NP + 1064 nm irradiation survives for 59 days without significant weight loss. Consistently, tumor apoptosis was examined through hematoxylin-eosin (H&E) staining and terminal deoxynucleotidyl transferase-mediated dUTP-biotin nick end labeling (TUNEL) assays. As shown in Figure 5D, significant apoptosis is observed in the group with NP +1064 nm irradiation, which is in remarkable contrast to the group with PBS, NP, and NP + 808 nm irradiation.

It is also worth noting that NP is safe. A single dose of NP (10 mg kg^{-1}) or PBS was intravenously injected into the healthy BALB/c mice (Figure S20A, Supporting Information), no noticeable difference could be found in the serum biochemistry, complete blood panels, body weight (Figure S20B,C, Supporting Information), and hematoxylin and eosin (H&E) staining of the main organ (Figure S21, Supporting Information) after the treatment.

3. Conclusion

We have developed a novel class of biodegradable polymeric PTAs with excellent photothermal conversion efficiency for tumor treatment, as demonstrated in a deep-seated ovarian cancer model. This work provides a novel design toward better PTAs for the effective treatment of tumors.

Supporting Information

Supporting Information is available from the Wiley Online Library or from the author.

Acknowledgements

The authors thank the financial support from the National Natural Science Foundation of China (51873218, 52003161, 52073015), the National Key Research and Development Program of Hunan Province of China (2019SK2251), the Natural Science Foundation of Jiangxi province of China (20192ACB70012). All animal experiments reported herein were performed under guidelines evaluated and approved by Peking University Institutional Animal Care and Use Committee (LA2021316).

Conflict of Interest

The authors declare no conflict of interest.

Data Availability Statement

Research data are not shared.

Keywords

biodegradability, NIR-II window, ovarian cancer model, photothermal agents, photothermal therapy

Received: August 2, 2021
Revised: October 10, 2021
Published online: November 28, 2021

[1] a) L. Cheng, C. Wang, L. Z. Feng, K. Yang, Z. Liu, *Chem. Rev.* **2014**, *114*, 10869; b) Y. J. Liu, P. Bhattarai, Z. F. Dai, X. Y. Chen, *Chem. Soc. Rev.* **2019**, *48*, 2053.

[2] a) M. W. Shi, Z. L. Fu, W. Pan, Y. Y. Chen, K. Y. Wang, P. Zhou, N. Li, B. Tang, *Angew. Chem., Int. Ed.* **2021**, *24*, 13564; b) H. Y. Wang, J. J. Chang, M. W. Shi, W. Pan, N. Li, B. Tang, *Angew. Chem., Int. Ed.* **2019**, *131*, 1069.

[3] a) L. N. Wang, Y. J. Yu, D. S. Wei, L. P. Zhang, X. Y. Zhang, G. X. Zhang, D. Ding, H. H. Xiao, D. Q. Zhang, *Adv. Mater.* **2021**, *33*, 2100599; b) X. J. Men, F. Wang, H. B. Chen, Y. B. Liu, X. X. Men, Y. Yuan, Z. Zhang, D. Y. Gao, C. F. Wu, Z. Yuan, *Adv. Funct. Mater.* **2020**, *30*, 1909673.

[4] a) C. L. Zhu, L. B. Liu, Q. Yang, F. T. Lv, S. Wang, *Chem. Rev.* **2012**, *112*, 4687; b) H. S. Jung, P. Verwilst, A. Sharma, J. Shin, J. L. Sessler, J. S. Kim, *Chem. Soc. Rev.* **2018**, *47*, 2280.

[5] a) B. Guo, Z. H. Sheng, D. H. Hu, C. B. Liu, H. R. Zheng, B. Liu, *Adv. Mater.* **2018**, *30*, 1802591; b) Y. C. Ma, Y. X. Zhang, X. Q. Li, Y. Y. Zhao, M. Li, W. Jiang, X. F. Tang, J. X. Dou, L. G. Lu, F. Wang, Y. C. Wang, *ACS Nano* **2019**, *13*, 11967.

[6] a) X. Z. Li, L. Liu, S. L. Li, Y. P. Wan, J.-X. Chen, S. Tian, Z. M. Huang, Y.-F. Xiao, X. Cui, C. Y. Xiang, Q. L. Tan, X.-H. Zhang, W. S. Guo,

X.-J. Liang, C.-S. Lee, *ACS Nano* **2019**, *13*, 12901; b) Y. Y. Jiang, J. C. Li, X. Zhen, C. Xie, K. Y. Pu, *Adv. Mater.* **2018**, *30*, 1705980.

[7] a) K. Hu, L. Xie, Y. D. Zhang, M. Hanyu, Z. M. Yang, K. Nagatsu, H. Suzuki, J. Ouyang, X. Y. Ji, J. J. Wei, H. Xu, O. C. Farokhzad, S. H. Liang, L. Wang, W. Tao, M. R. Zhang, *Nat. Commun.* **2020**, *11*, 2778; b) M. M. Luo, T. J. Fan, Y. Zhou, H. Zhang, L. Mei, *Adv. Funct. Mater.* **2019**, *29*, 1808306.

[8] H. Y. Wang, X. T. Pan, X. T. Wang, W. W. Wang, Z. J. Huang, K. Gu, S. Liu, F. R. Zhang, H. Y. Shen, Q. P. Yuan, J. Ma, W. Yuan, H. Y. Liu, *ACS Nano* **2020**, *14*, 2847.

[9] S. L. Li, Q. Y. Deng, Y. C. Zhang, X. Z. Li, G. H. Wen, X. Cui, Y. P. Wan, Y. W. Huang, J. X. Chen, Z. H. Liu, L. D. Wang, C.-S. Lee, *Adv. Mater.* **2020**, *32*, 2001146.

[10] B. Liu, C. X. Li, G. Y. Chen, B. Liu, X. R. Deng, Y. Wei, J. Xia, B. G. Xing, P. a. Ma, J. J. Lin, *Adv. Sci.* **2017**, *4*, 1600540.

[11] a) S. L. Li, X. Y. Wang, R. Hu, H. Chen, M. Li, J. W. Wang, Y. X. Wang, L. B. Liu, F. T. Lv, X. J. Liang, S. Wang, *Chem. Mater.* **2016**, *28*, 8669; b) Y. Y. Cao, J.-H. Dou, N.-j. Zhao, S. M. Zhang, Y.-Q. Zheng, J.-P. Zhang, J.-Y. Wang, J. Pei, Y. P. Wang, *Chem. Mater.* **2017**, *29*, 718.

[12] a) L. G. Xu, L. Cheng, C. Wang, R. Peng, Z. Liu, *Polym. Chem.* **2014**, *5*, 1573; b) H. Sun, F. T. Lv, L. B. Liu, Q. Gu, S. Wang, *Adv. Ther.* **2018**, *1*, 1800057; c) B. L. Guo, L. Glavas, A.-C. Albertsson, *Prog. Polym. Sci.* **2013**, *38*, 1263.

[13] a) J. C. Li, J. H. Rao, K. Y. Pu, *Biomaterials* **2018**, *155*, 217; b) Kenry, B. L. , *Biomacromolecules* **2018**, *19*, 1783.

[14] a) X. S. Li, J. F. Lovell, J. Y. Yoon, X. Y. Chen, *Nat. Rev. Clin. Oncol.* **2020**, *17*, 657; b) Y. Lyu, C. Xie, S. A. Chechetka, E. Miyako, K. Y. Pu, *J. Am. Chem. Soc.* **2016**, *138*, 9049.

[15] a) C. Gao, F. Tang, J. X. Zhang, S. M. Y. Lee, R. B. Wang, *J. Mater. Chem. B* **2017**, *5*, 2337; b) D. S. Wei, Y. J. Yu, X. C. Zhang, Y. H. Wang, H. Chen, Y. Zhao, F. Y. Wang, G. H. Rong, W. W. Wang, X. Kang, J. Cai, Z. H. Wang, J.-Y. Yin, M. Hanif, Y. B. Sun, G. F. Zha, L. X. Li, G. H. Nie, H. H. Xiao, *ACS Nano* **2020**, *14*, 16984.

[16] C. V. Smith, D. P. Jones, T. M. Guenthner, L. H. Lash, B. H. Lauterburg, *Toxicol. Appl. Pharmacol.* **1996**, *140*, 1.

[17] Y. Y. Jiang, X. H. Zhao, J. G. Huang, J. C. Li, P. K. Upputuri, H. Sun, X. Han, M. Pramanik, Y. S. Miao, H. W. Duan, K. Y. Pu, R. P. Zhang, *Nat. Commun.* **2020**, *11*, 1857.

[18] a) J.-L. Wang, X.-J. Du, J.-X. Yang, S. Shen, H.-J. Li, Y.-L. Luo, S. Iqbal, C.-F. Xu, X.-D. Ye, J. Cao, J. Wang, *Biomaterials* **2018**, *182*, 104; b) X. Yang, Y. J. Yu, X. Huang, Q. X. Chen, H. Wu, R. Wang, R. G. Qi, Y. F. Miao, Y. M. Qiu, *Mater. Sci. Eng., C* **2019**, *96*, 96; c) C. L. Hofmann, M. C. O'Sullivan, A. Detappe, Y. Yu, X. Yang, W. Qi, C. D. Landon, M. J. Therien, M. W. Dewhirst, P. P. Ghoroghchian, G. M. Palmer, *Nanoscale* **2017**, *9*, 13465.

[19] L. L. Dong, G. M. Ji, Y. Liu, X. Xu, P. P. Lei, K. M. Du, S. Y. Song, J. Feng, H. J. Zhang, *Nanoscale* **2018**, *10*, 825.

[20] M. B. Zheng, P. F. Zhao, Z. Y. Luo, P. Gong, C. F. Zheng, P. F. Zhang, C. X. Yue, D. Y. Gao, Y. F. Ma, L. T. Cai, *ACS Appl. Mater. Interfaces* **2014**, *6*, 6709.

[21] a) S. Domcke, R. Sinha, D. A. Levine, C. Sander, N. Schultz, *Nat. Commun.* **2013**, *4*, 2126; b) M. Javellana, C. Hoppenot, E. Lengyel, *Gynecol. Oncol.* **2019**, *152*, 228.

[22] S. Gao, G. G. Wei, S. H. Zhang, B. B. Zheng, J. J. Xu, G. X. Chen, M. W. Li, S. L. Song, W. Fu, Z. Y. Xiao, W. Lu, *Nat. Commun.* **2019**, *10*, 2206.

[23] Z. Tao, M. D. Muzumdar, A. Detappe, X. Huang, E. S. Xu, Y. Yu, T. H. Mouhieddine, H. Song, T. Jacks, P. P. Ghoroghchian, *Nano Lett.* **2018**, *18*, 2195.